Focus-extension by depth-encoded synthetic aperture in Optical Coherence Tomography

Jianhua Mo, Mattijs de Groot, and Johannes F. de Boer[*]

Institute for Lasers, Life and Biophotonics Amsterdam, Department of Physics and Astronomy, VU University Amsterdam, De Boelelaan 1081, 1081 HV Amsterdam, The Netherlands
[*]jfdeboer@few.vu.nl

Abstract: We present a novel method to extend the depth-of-focus of Optical Coherence Tomography (OCT). OCT is an interferometric imaging technique that provides depth-resolved scattering information. The axial resolution in OCT is provided by the coherence gate and is invariant over the full image depth. The lateral resolution is determined by the beam parameters such as wavelength and numerical aperture. The Rayleigh range determines the depth range over which the lateral resolution can be maintained. The lateral resolution is often sacrificed to maintain relatively long Rayleigh range. In this study, we propose to use a depth-encoded synthetic aperture detection scheme to extend the depth range over which a sharp focus can be maintained beyond the Rayleigh range. An annular phase plate is inserted into the light path in the sample arm, which gives rise to three separate images in a single B-scan, corresponding to three different optical path length encoded apertures. These three images are coherently summed after phase-manipulation to reconstruct a new image with a lateral resolution that is maintained over a five times larger depth range.

References and links

1. D. Huang, E. A. Swanson, C. P. Lin, J. S. Schuman, W. G. Stinson, W. Chang, M. R. Hee, T. Flotte, K. Gregory, C. A. Puliafito, and et, "Optical coherence tomography," Science **254**(5035), 1178–1181 (1991).
2. J. A. Izatt, M. R. Hee, E. A. Swanson, C. P. Lin, D. Huang, J. S. Schuman, C. A. Puliafito, and J. G. Fujimoto, "Micrometer-scale resolution imaging of the anterior eye in vivo with optical coherence tomography," Arch. Ophthalmol. **112**(12), 1584–1589 (1994).
3. Z. Chen, T. E. Milner, D. Dave, and J. S. Nelson, "Optical Doppler tomographic imaging of fluid flow velocity in highly scattering media," Opt. Lett. **22**(1), 64–66 (1997).
4. B. E. Bouma, G. J. Tearney, C. C. Compton, and N. S. Nishioka, "High-resolution imaging of the human esophagus and stomach in vivo using optical coherence tomography," Gastrointest. Endosc. **51**(4), 467–474 (2000).
5. C. E. Saxer, J. F. de Boer, B. H. Park, Y. Zhao, Z. Chen, and J. S. Nelson, "High-speed fiber based polarization-sensitive optical coherence tomography of in vivo human skin," Opt. Lett. **25**(18), 1355–1357 (2000).
6. B. Braaf, K. A. Vermeer, V. A. D. P. Sicam, E. van Zeeburg, J. C. van Meurs, and J. F. de Boer, "Phase-stabilized optical frequency domain imaging at 1-µm for the measurement of blood flow in the human choroid," Opt. Express **19**(21), 20886–20903 (2011).
7. G. J. Tearney, S. Waxman, M. Shishkov, B. J. Vakoc, M. J. Suter, M. I. Freilich, A. E. Desjardins, W. Y. Oh, L. A. Bartlett, M. Rosenberg, and B. E. Bouma, "Three-dimensional coronary artery microscopy by intracoronary optical frequency domain imaging," JACC Cardiovasc. Imaging **1**(6), 752–761 (2008).
8. E. A. Swanson, D. Huang, M. R. Hee, J. G. Fujimoto, C. P. Lin, and C. A. Puliafito, "High-speed optical coherence domain reflectometry," Opt. Lett. **17**(2), 151–153 (1992).
9. J. M. Schmitt, S. L. Lee, and K. M. Yung, "An optical coherence microscope with enhanced resolving power in thick tissue," Opt. Commun. **142**(4-6), 203–207 (1997).
10. B. Qi, A. P. Himmer, L. M. Gordon, X. D. V. Yang, L. D. Dickensheets, and I. A. Vitkin, "Dynamic focus control in high-speed optical coherence tomography based on a microelectromechanical mirror," Opt. Commun. **232**(1-6), 123–128 (2004).

11. B. A. Standish, K. K. Lee, A. Mariampillai, N. R. Munce, M. K. Leung, V. X. Yang, and I. A. Vitkin, "In vivo endoscopic multi-beam optical coherence tomography," Phys. Med. Biol. **55**(3), 615–622 (2010).
12. Z. Ding, H. Ren, Y. Zhao, J. S. Nelson, and Z. Chen, "High-resolution optical coherence tomography over a large depth range with an axicon lens," Opt. Lett. **27**(4), 243–245 (2002).
13. R. A. Leitgeb, M. Villiger, A. H. Bachmann, L. Steinmann, and T. Lasser, "Extended focus depth for Fourier domain optical coherence microscopy," Opt. Lett. **31**(16), 2450–2452 (2006).
14. L. Liu, C. Liu, W. C. Howe, C. J. R. Sheppard, and N. Chen, "Binary-phase spatial filter for real-time swept-source optical coherence microscopy," Opt. Lett. **32**(16), 2375–2377 (2007).
15. T. S. Ralston, D. L. Marks, P. S. Carney, and S. A. Boppart, "Interferometric synthetic aperture microscopy," Nat. Phys. **3**(2), 129–134 (2007).
16. Y. Yasuno, J.-i. Sugisaka, Y. Sando, Y. Nakamura, S. Makita, M. Itoh, and T. Yatagai, "Non-iterative numerical method for laterally superresolving Fourier domain optical coherence tomography," Opt. Express **14**(3), 1006–1020 (2006).
17. L. Yu, B. Rao, J. Zhang, J. Su, Q. Wang, S. Guo, and Z. Chen, "Improved lateral resolution in optical coherence tomography by digital focusing using two-dimensional numerical diffraction method," Opt. Express **15**(12), 7634–7641 (2007).
18. M. de Groot, C. L. Evans, and J. F. de Boer, "Self-interference fluorescence microscopy: three dimensional imaging without depth scanning," Opt. Express **20**(14), 15253–15262 (2012).
19. D. M. de Bruin, R. H. Bremmer, V. M. Kodach, R. de Kinkelder, J. van Marle, T. G. van Leeuwen, and D. J. Faber, "Optical phantoms of varying geometry based on thin building blocks with controlled optical properties," J. Biomed. Opt. **15**(2), 025001 (2010).
20. J. Li, M. de Groot, F. Helderman, J. Mo, J. M. A. Daniels, K. Grünberg, T. G. Sutedja, and J. F. de Boer, "High speed miniature motorized endoscopic probe for optical frequency domain imaging," Opt. Express **20**(22), 24132–24138 (2012).
21. I. Grulkowski, J. J. Liu, B. Potsaid, V. Jayaraman, J. Jiang, J. G. Fujimoto, and A. E. Cable, "High-precision, high-accuracy ultralong-range swept-source optical coherence tomography using vertical cavity surface emitting laser light source," Opt. Lett. **38**(5), 673–675 (2013).

1. Introduction

Optical coherence tomography (OCT) is an interferometric technique that provides cross-sectional images of biological tissue [1]. It has become an essential tool for clinical diagnosis and disease monitoring in ophthalmology and it shows great potential in other clinical areas such as dermatology, cardiology and gastroenterology [2–7]. The axial resolution of OCT imaging at moderate numerical aperture is determined primarily by the light source as illustrated by the equation: $\delta L = 2 \ln(2) \lambda_c^2 / \pi \Delta\lambda$ where λ_c and $\Delta\lambda$ are the central wavelength and the optical bandwidth of the source, respectively [8]. The transverse resolution depends on the wavelength λ and beam size (d) of the laser light as well as the objective's focal length (f). In the focus, the lateral resolution is given by the focus diameter: $\Delta r = 4\lambda f / \pi d$. The single-sided depth range over which the lateral resolution is maintained within a factor of $\sqrt{2}$ is given by the Rayleigh range ($z_R = \pi \Delta r^2 / 4\lambda$). The depth of focus is generally defined as twice the Rayleigh range. Current broadband laser sources permit axial resolutions below 10 μm over several millimeters of image depth. However, it is impossible to achieve ~10 μm transverse resolution over a depth range of several millimeters using Gaussian beams and normal objectives. The relatively short focal-depth of imaging optics limits the application of high lateral resolution OCT to thin slices.

To date, various methods have been proposed to address the limited depth-of-focus of OCT imaging. Examples are dynamic focus [9, 10], multi-focus [11] and focal-depth extension methods [12–17]. Dynamic focusing synchronizes the focal plane position with coherence gate scanning, which is more suitable for time-domain OCT [9, 10]. The multi-focus approach requires parallel acquisition at different focal depths [11]. In comparison, depth-of-focus extension has been more successful. Till now, the methods proposed for focus-depth extension can be categorized into three groups: (1) Bessel beam illumination with an axicon lens [12, 13], (2) phase apodization [14] and (3) digital refocusing [15–17]. The axicon and phase apodization approaches are inefficient in illumination and collection from the extended focus, leading to signal losses of tens of decibels [13, 14]. Interferometric synthetic aperture methods (ISAM) have been developed for digital refocusing by solving the inverse

scattering problem [15]. It is computationally expensive and requires phase stable acquisition of consecutive depth profiles. Other digital refocusing methods based on deconvolution or scalar diffraction models also require phase-stable OCT measurements [16, 17].

In this study, we propose a novel method to extend the focus-depth, which is compatible with endoscopy and computationally inexpensive. It is analogous to synthetic aperture radar. The idea is to use an annular phase plate to separate the light into different optical apertures that are encoded by a depth offset in an OCT A-scan. This leads to the acquisition of multiple OCT images in parallel in a single B-scan. Manipulation of the phase of these images and coherent summation allows the construction of a new image with a significantly extended depth-of-focus.

2. Principle of depth-encoded synthetic aperture OCT
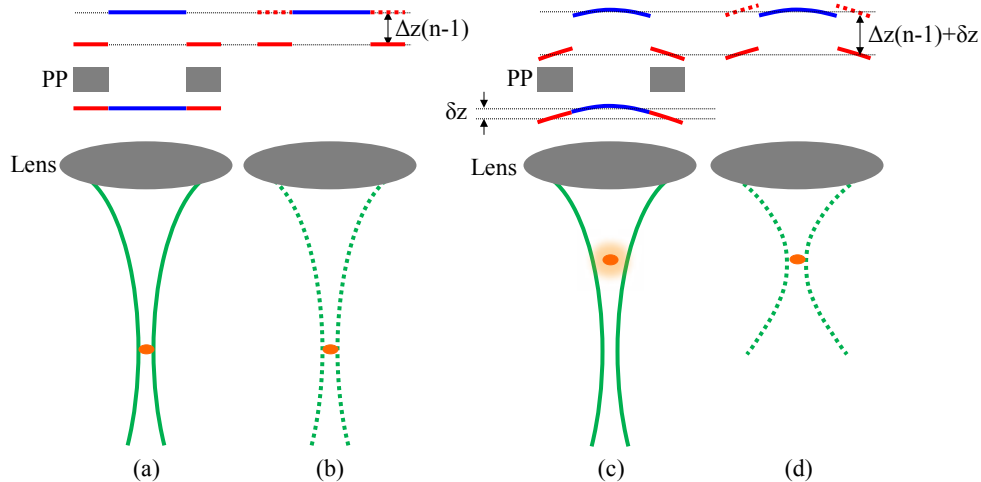

Fig. 1. Principle of the depth-encoded synthetic aperture method for extending the depth-of-focus of optical coherence tomography. The drawing shows the source of the scattered light (orange dot), the lens, the beam diameter as a function of the axial position defined by Gaussian optics (solid green), the reconstructed beam diameter after image processing (dotted green), the wavefronts before and after the phase plate (blue and red lines) in Figs. (a) and (c). Δz and n are the thickness and refractive index of the annular phase plate (PP). (a) The scattering object is located in the focus of the lens. Solid blue and red lines indicate the sections of the wavefront that pass through the inner and outer sections of the annular phase plate, respectively. The outer section is delayed by a term $\Delta z(n-1)$. (b) By application of the Fourier shift theorem, the delayed part of the wavefront is shifted back (dotted red lines) and the original image is reconstructed. (c) When the scattering object is out of focus (here above the focal plane) the wavefront is curved. This leads to a small extra optical path length difference δz. (d) By compensating both the shift $\Delta z(n-1)$ induced by the phase plate and the extra term δz a refocused image with improved lateral resolution (indicated by the dotted green lines) can be obtained. See section 2.1 for details.

An intuitive description of the principle of this novel depth-encoded synthetic aperture method is illustrated in Fig. 1. In section 2.1 a more thorough mathematical description is given. To explain the method, the wavefront of the scattered field is analyzed. An annular phase plate is inserted into the sample arm at the back focal plane of the imaging lens. The annular phase plate consists of a 3-mm thick polycarbonate plate with a circular hole at the center. Approximately half of the scattered light travels through the central hole (central beam), and half of the light travels through the polycarbonate plate (edge beam). When the object is in-focus, the collected light goes through the phase plate with a planar wavefront. The edge beam is delayed with respect to the central beam due to the longer optical path length, given by $\Delta z(n-1)$, with Δz the thickness of the phase plate, and n the refractive

index of the phase plate (Fig. 1(a)). In a single OCT B-scan, the central beam image and the edge beam image are encoded to two different depth locations separated by $\Delta z(n-1)$. A new image can be constructed by correcting the delay (or depth-separation $\Delta z(n-1)$) and coherently adding those two images (Fig. 1(b)). The newly constructed image has a comparable lateral resolution as the image acquired without the phase plate. When the object is defocused (Fig. 1(c)) (in this example above the focal plane), the edge beam undergoes the same delay due to the phase plate as in the in-focus case. In addition, a small extra delay (δz) occurs due to the curvature of the wavefront. This small extra delay is equivalent to the delay as described in our earlier publication on self interference fluorescence microscopy (SIFM) [18]. An image with improved focus can be constructed by correcting the edge beam wavefront for both the terms $\Delta z(n-1)$ and δz (Fig. 1(d)).

2.1 Theory

Mathematically, the detected OCT signal $I(k)$ in spectral domain OCT and optical frequency domain imaging (OFDI) for a single scattering object can be expressed by the following equation:

$$I(k) = I_r(k) + I_s(k) + 2\sqrt{I_r(k)I_s(k)}\alpha\cos(2kz). \tag{1}$$

where k is the wave number, α is the square root of the scattering object reflectivity at depth z. $I_r(k)$ and $I_s(k)$ on the right-hand side of Eq. (1) are the wavelength-dependent intensity reflected from the reference arm and sample arm, respectively, and are also called DC terms. The third term is the interference between the reference arm and sample arm that contains the depth information. The DC terms are from now on omitted since they carry no depth information and only the interference term is retained.

When a phase plate is inserted into the sample arm, there are three different paths for the sample arm light to reach the detector *via* a scattering object in the sample: the first light path passes through the center of the phase plate both on the way to the scattering object and back. The second path passes through the center on the way to the scattering object and travels back through the edge, or, equivalently, passes through the edge on the way to the scattering object and travels back through the center. Finally, the third light path passes through the edge of the phase plate both on the way to the scattering object and back.

These three paths create three different depth encoded images, where each image corresponds to the light detected through a distinct circular (or annular) aperture. The interference of the sample arm light with a local oscillator field (the reference field) provides both the amplitude and phase of these three images. By adding these three images coherently, and manipulating the phase in a way similar to synthetic aperture radar or phased array ultrasonics, a single image can be constructed for which the lateral resolution is preserved over a much larger range than the Rayleigh range of the original Gaussian beam.

The interference term for a single object with the phase plate in the beam path is thus given by:

$$
\begin{aligned}
I(k) = \sqrt{I_r(k)I_s(k)}\alpha\Big\{\big[&\exp(i2kz)\ldots \\
&+ \exp(i2kz + ik(\Delta z(n-1)+\delta z))\ldots \\
&+ \exp(i2kz + ik2(\Delta z(n-1)+\delta z))\big] + C.C.\Big\}.
\end{aligned}
\tag{2}
$$

where $\Delta z(n-1)$ is the single pass optical path length difference between the central beam and edge beam, C.C. indicates the complex conjugate, and δz is the small extra optical path

length difference between the central beam and edge beam resulting from the defocus-induced wavefront curvature, which becomes zero when the object is in focus.

To facilitate the image processing of summing coherently the three terms in Eq. (2) into a single image, the k value is written as $k = k_0 + \Delta k$ for the terms that contain products with Δz and δz. As an example, the second term on the right hand side of Eq. (2) (the middle image) can be rewritten as:

$$I(k) = \sqrt{I_r(k)I_s(k)}\alpha \exp(i2kz)\exp\left(ik_0\Delta z(n-1) + ik_0\delta z + i\Delta k\Delta z(n-1) + i\Delta k\delta z\right) + C.C.. \quad (3)$$

The wavelength-dependent phase term ($\Delta k\delta z$) can be neglected since δz is smaller than a wavelength, and the optical bandwidth or the tuning range of the laser source is in general smaller than ± 5% of the central wavelength. Then, Eq. (3) can be written as follows with the constant phase (k-independent) terms separated out:

$$I(k) = \exp\left(i\psi_{middle}\right)\sqrt{I_r(k)I_s(k)}\alpha \exp\left(i2kz\right)\exp\left(i\Delta k\Delta z(n-1)\right) + C.C..$$
$$with \ \psi_{middle} = k_0\Delta z(n-1) + k_0\delta z \quad (4)$$

The third term on the right hand side of Eq. (2) (the bottom image) is now given by:

$$I(k) = \exp(i\psi_{bottom})\sqrt{I_r(k)I_s(k)}\alpha \exp\left(i2kz\right)\exp\left(i2\Delta k\Delta z(n-1)\right) + C.C..$$
$$with \ \psi_{bottom} = 2k_0\Delta z(n-1) + 2k_0\delta z \quad (5)$$

compared to Eq. (1) for the OCT signal detected without phase plate, an extra oscillation phase ($\Delta k\Delta z(n-1)$) and a constant phase ψ are added in Eqs. (4) and (5), resulting from the phase plate and defocus effect. The phase term ($k_0\delta z$) is negative when the focal plane is below the imaging target and positive when the focal plane is above the imaging target. We hypothesize that the focus can be recovered by correcting the defocus-induced $k_0\delta z$ in the detected OCT signal.

2.2 Physical optics simulation

To explore the relationship between the phase factor $k_0\delta z$ and the defocus distance we performed a physical optics simulation using Zemax software (Radiant Zemax, Redmond, WA, USA). The simulation model (Fig. 2(a)) comprises: (1) a Gaussian source with a $1/e^2$ diameter of 9.2 μm in a medium with refractive index 1.44 to simulate the average refractive index of the phantom described in section 3, (2) an 18 mm focal length objective (LSM02, Thorlabs, Newton, NJ, USA) to collect the light, (3) a zone plate to simulate the annular phase plate (optical thickness: 0.68 mm and a hole with a diameter of 1.8 mm), (4) a collimator (focal length: 18.67 mm) to couple the light into the fiber and (5) a collection fiber (mode field diameter: 9.2 μm). This model was used to calculate the total coupling efficiency of the light from the point source to the single mode fiber as a function of wavelength and defocus distance [18]. Figure 2(b) presents an example of the coupling efficiency as a function of wavelength. It shows constructive and destructive interference over the source spectrum caused by the optical path length difference for the core and edge beams through the phase plate. Because of the defocus-induced phase factor $k_0\delta z$, the phase of this interference pattern shifts when the point source is moved away from the focal plane (Fig. 2(b)). As shown in Fig. 2(c), the phase shift is linearly dependent on the defocus within a region of approximately 400 μm around the focal plane. This corresponds to a region of approximately 3.5 times the Rayleigh length. The slope of the curve in the linear region is 7.25 mrad/μm. The physical optics model thus predicts a slope of 7.25 mrad/μm for the defocus induced phase shift of the middle image (single pass through the edge of the phase plate). Since for the

bottom image the light travels twice through the edge of the phase plate, a slope of 14.5 mrad/μm is expected. The sinusoidal modulation of the coupling efficiency as a function of wavelength (Fig. 2(b)), introduced by the phase plate, indicates that the phase plate reduces the OCT signal by 50%.
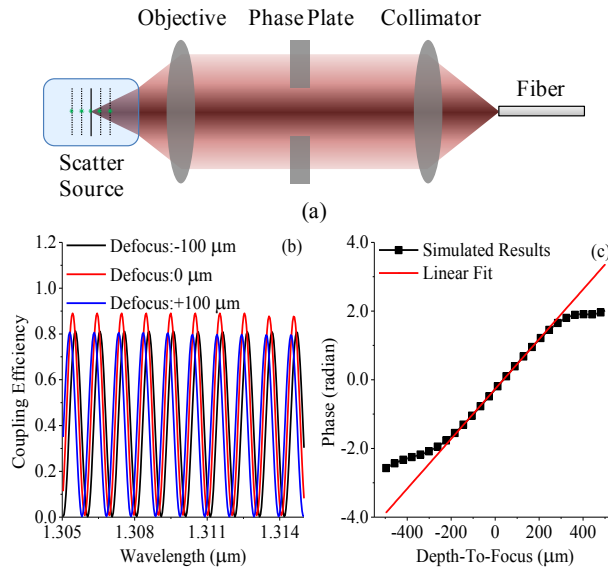

Fig. 2. (a) Physical optics model including the lenses, the medium, the collection fiber and the phase plate. (b) Coupling efficiency as a function of wavelength for three different positions of the source with respect to the focal plane. (c) Phase shift of the coupling efficiency function in (b) as a function of defocus. The slope of the linear region is 7.25 mrad/μm.
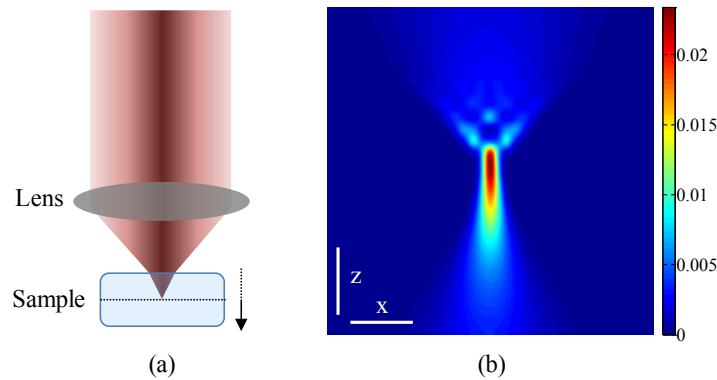

Fig. 3. Light intensity distribution of the focused beam in the sample. (a) The lateral and depth intensity distribution is evaluated at the plane indicated by the dotted line as a function of axial location of the sample with respect to the lens. (b) Color coded intensity distribution as a function over x (lateral) and z (depth) dimensions. The image is normalized to each row for better visibility of the lateral structure. Scale bars are 20 μm in x dimension and 200 μm in z dimension.

In addition, we also simulated the point spread function (PSF) of the light beam at different defocused positions without the phase plate to determine the exact intensity distribution. To simulate the experimental situation, a 300-μm thick layer with refractive index of 1.44 is defined in the physical optics model as shown in Fig. 3(a); then the irradiance cross-section, also called PSF, on a surface in the middle of the layer is calculated as the layer is moved away from the lens along the optical axis. The calculated PSF is convolved with a

Gaussian window which has a 5-µm width (diameter of the spheres used in experiment) to enable a good comparison between experiment and simulation. This yields the single pass PSF. In order to account for the PSF of both the incident and the scattered beam Fig. 3(b) shows the squared irradiance along lateral (x) and axial (z) dimensions. Below the focal plane the lateral intensity distribution shows the expected profile for a focused Gaussian beam, but above the focal plane (between objective and focal plane), the lateral intensity distribution exhibits multiple-maxima.
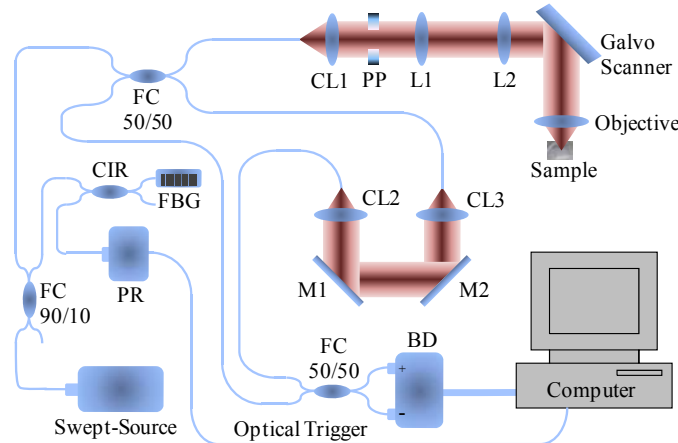
3. Experiment setup

Fig. 4. Schematic of Optical Frequency Domain Imaging (OFDI) system. PP: Annular Phase Plate; FC: Fiber-optic Coupler; CIR: Fiber-optic Circulator; CL: Collimator; L: Lens; M: Mirror; FBG: Fiber Bragg Grating; PR: Photoreceiver; BD: Balanced Detector

The in-house-built OFDI system consists of a wavelength-swept laser source, sample and reference arms, galvo mirror scanning system, optical trigger generation and data acquisition card as shown in Fig. 4. The light source centered at 1310 nm sweeps from 1258 to 1366 nm at a frequency of 50 KHz (Axsun Technologies Inc., MA, USA). The output power of the laser light is about 29 mW. The light from the source is split by a 90/10 fiber coupler. A small portion (10%) is sent to a fiber bragg grating (FBG, 1269.86 nm, O/E land Inc., LaSalle, QC, CA) and the reflected light is detected by a photoreceiver (model 1811, 125-MHz, New Focus, San Jose, CA, USA) to generate an optical trigger pulse. The large portion (90%) is further split into the sample arm (50%) and the reference arm (50%) by a 50/50 fiber coupler. The back-reflected light from the sample arm is collected by the same coupler and transferred to another 50/50 fiber coupler for balanced-detection with a balanced amplified photo-detector (PDB430C, 800~1700 nm, 350 MHz, Thorlabs, Newton, NJ, USA). The light in the reference arm is coupled to the aforementioned 50/50 coupler after a free space delay line to match the reference and sample arm path length. A special optical coherence tomography scanning lens with 18 mm focal length (LSM02, Thorlabs, Newton, NJ, USA) is used for delivering the laser light to the sample and collecting the back-scattered photons. The annular phase plate (PP) is fabricated by drilling a 1.8 mm (diameter) hole in the center of a transparent polycarbonate slide of 3 mm thickness. It is positioned at the back focal plane of the scanning objective which is relayed from the objective by a pair of achromatic lenses with a focal length of 60 mm.

Lateral scanning is implemented through a galvo mirror scanning system which is driven by a 16-bit analog voltage output device (PCIe-6259, National Instruments, Austin, TX, USA). Saw-tooth waveforms are generated by PCIe-6259 and sent to the galvo-scanner driver board for raster scanning. The OCT signal detected by the balanced detector is filtered by a low pass filter (BLP-70+, Mini-circuits, Brooklyn, NY, USA) to block any signals at

frequencies higher than 70 MHz. Then, it is digitized by a 12-bit PCI express digitizer (ATS9350, Alazar Technologies Inc., Pointe Claire, QC, CA). The digitizer is driven by an external k-clock (96~137 MHz) provided by the laser source. This ensures the spectrum is linearly sampled in k-space which allows for direct Fourier transformation of the measured spectrum. Each A-scan is triggered by an optical trigger instead of the sweep trigger provided by the laser source. This is done to avoid phase-errors resulting from jitter on the sweep trigger. Data acquisition, galvo scanning control and real-time display was implemented in LabVIEW (National Instruments, Austin, TX, USA).

A phantom was created by embedding 5-μm melamine spheres into a silicone polymer [19]. Since the depth range of the systems was 5-mm in air, the phantom was made 300 μm thick (optical thickness: 432 μm). This ensured that three images from different optical apertures could be depth-encoded without overlap. In the experiment, the focal plane was initially positioned below the phantom and then the phantom was translated away from the objective, along the optic axis, in steps of 40 μm. B-scans were acquired at each depth.
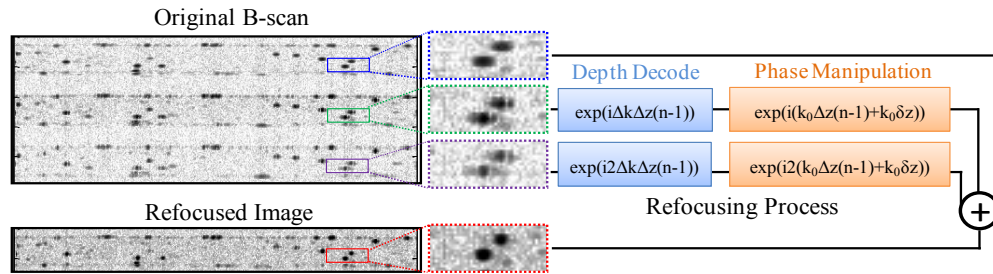
4. Results

Fig. 5. Refocusing Process: A single B-scan contains three images of the same object at different depths (i.e., top, middle and bottom); the first step is to correct the depth-separation due to the phase plate for the middle and bottom images (blue text box). Then, the phase of the middle and bottom images are further manipulated (orange text box) and coherently added to the top image to construct a new image with improved lateral resolution. The four colored windows are zoomed-in images of two spheres to better visualize the refocusing process. The image is 1.28 mm wide and its aspect ratio is 3:1.

Figure 5 shows an experimental OCT image of the scattering sample with the annular phase plate and the result of the refocusing process. The phantom was defocused by about 1.5 times the Rayleigh range. The original B-scan on the left side of Fig. 5 contains three depth-encoded images corresponding to three different apertures. These three separated images are coherently added after applying the refocusing algorithm. The refocusing algorithm consists of two steps:

(1) The first step is to depth-decode the middle and bottom images to the depth position of the top image to correct the depth-offset due to the phase plate ($\Delta z(n-1)$). This can be done using the Fourier shift-theorem:

$$I_T(k) = I(k)\exp(i\Delta k\Delta\phi). \qquad (6)$$

where $I(k)$ and $I_T(k)$ are the spectrum before and after the frequency-shift, respectively; and $\Delta\phi$ is the frequency-shift factor for depth-decoding the middle and bottom images relative to the top image in the spectral domain. Based on the theoretical description from section 2 we expect that $\Delta\phi$ is equal to $\Delta z(n-1)$ for the middle image and to $2\Delta z(n-1)$ for the bottom image. Experimentally, we estimated frequency-shift factor ranges for both middle image and bottom image according to the optical thickness of the phase plate. Next, over a dense 2-D mesh of frequency-shift factors for the middle and bottom images, we calculated

the sum of the magnitude of the top image with the shifted middle and bottom images (incoherent magnitude sum) and then squared the magnitude. The optimal frequency-shift factor was determined by maximizing the squared magnitude integrated over the incoherently summed image. The ratio of the optimal frequency-shift factors for the bottom and middle images was 1.9996 ± 0.0017.

(2) The second step is to correct the defocus-induced additional phase change ψ. This phase change is wavenumber-independent and therefore can be corrected simply by applying a constant phase factor to the Fourier-transformed spectrum which undergoes a frequency-shift in the first step. Then, all three complex images are coherently summed to reconstruct a new image. This can be expressed as:

$$S_{refocused} = S_{top} + S_{middle} \exp(-i\psi_{middle}) + S_{bottom} \exp(-i\psi_{bottom}). \tag{7}$$

where S_{top} is the original complex Fourier-transformed spectrum, S_{middle} and S_{bottom} are the complex Fourier-transformed spectra that were depth-decoded in step 1, ψ_{middle} and ψ_{bottom} are phase factors in the range of 0 to 2π applied to S_{middle} and S_{bottom}, respectively. In principle, ψ_{middle} and ψ_{bottom} are the wrapped phase of $k_0 \Delta z (n-1) + k_0 \delta z$ and $2(k_0 \Delta z(n-1) + k_0 \delta z)$. To determine ψ_{middle} and ψ_{bottom}, we calculate the coherent sum (complex sum) of the top, middle and bottom images for each possible combination of ψ_{middle} and ψ_{bottom}. The optimal values for ψ_{middle} and ψ_{bottom} are determined by maximizing the squared absolute value of the coherent sum (which is the backscattered intensity) integrated over the target depth range of the reconstructed or refocused image ($S_{refocused}$). The images with two spheres as an example in the colored windows in Fig. 5 provide detailed insight into the reconstruction process and how the focus is improved. The phase manipulation leads to constructive interference on the center part of the focus spot and destructive interference on the edge part of the focus spot (i.e., side lobe in middle and bottom images). This combined constructive and deconstructive interference process improves the lateral resolution and also increases the total backscattered intensity of the refocused image.

Figure 6 is a direct comparison between three different imaging modes for different positions of the lens focus: 1) the full beam image without phase plate, 2) the truncated Gaussian beam image (top image of the original B-scan), and 3) the refocused image, where the three images are shown as the top, middle and bottom in each subfigure. The subfigures (Figs. 6(a)-6(h)) represent the images of the phantom being moved away from the objective at 80-μm step size. Images were acquired with 40-μm step size but not all images are shown due to limited space. Due to the refractive index mismatch, the step size should be scaled by the refractive index of the phantom to represent the actual focal plane shift [9]. Thus, the physical phantom movement of 80 μm leads to a 115.2-μm displacement of the focal plane. From Figs. 6(a) to 6(h), it is seen that the spheres in the truncated beam images appeared to have a very slow change in width over the defocus process. This can be explained by the fact that the light beam is truncated from 3.4 mm to 1.8 mm (diameter) by the phase plate which results in an extension of Rayleigh range at the cost of an increased lateral focal spot size.
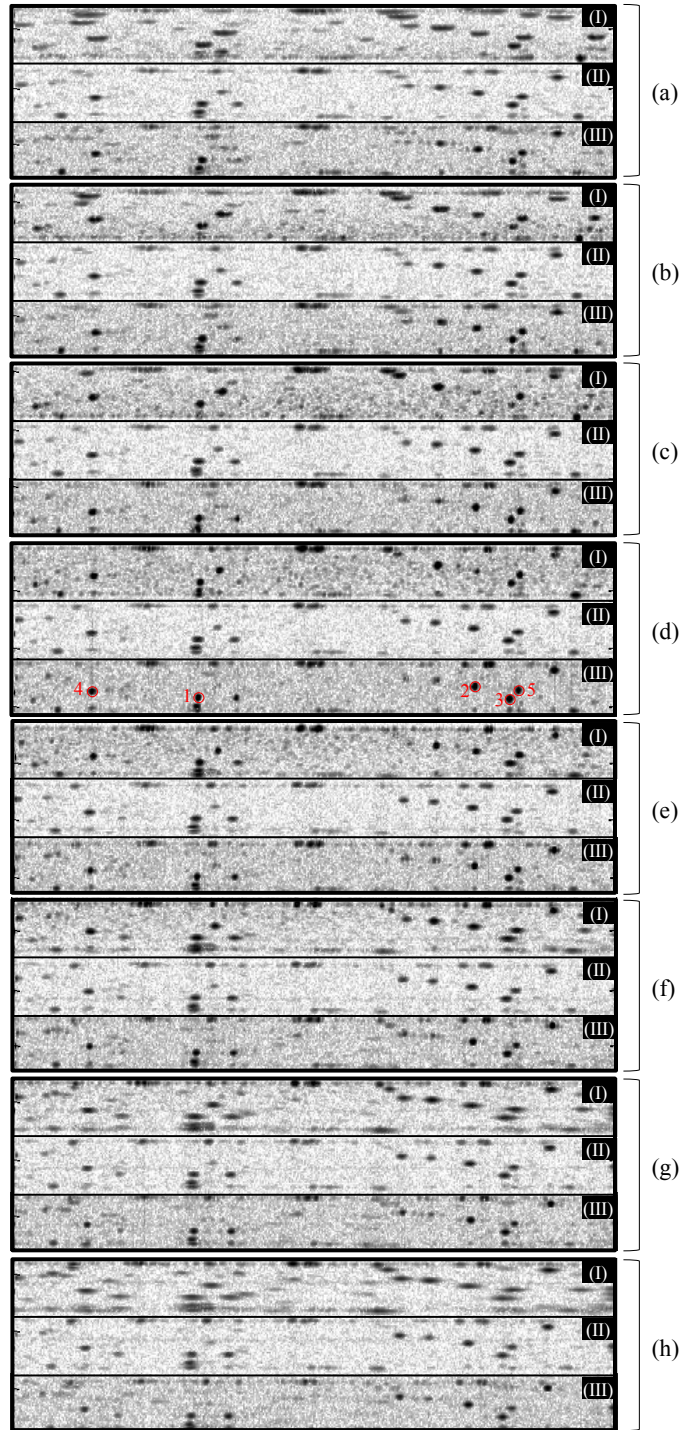
Fig. 6. (a)-(h): Intensity images acquired when the phantom is moved away from the objective at a physical step size of 80 μm. Each subfigure includes three imaging modes: (I) full beam image at top, (II) truncated Gaussian beam image at middle, and (III) refocused image at bottom. All the images are presented on a logarithmic scale with the colormap clipped to 75% of the maximum intensity of the image. The image is 1.28 mm wide and its aspect ratio is 3:1.

In contrast, the corresponding full beam image without phase plate experienced a much more rapid change in the sphere's width during the same defocus process. For the refocused images, it is obvious that as compared to the full beam image, the refocused image had comparable focus size and maintained the focus over a much larger depth range.

To better evaluate the performance of the refocusing algorithm we selected five spheres and labeled them with numbers 1 to 5 in Fig. 6(d). These were used as examples to quantify the focus performance. Figure 7 shows the spheres' intensity profiles on a linear scale and normalized for better comparison. From top to bottom row profiles are shown as a function of the translation of the phantom away from the objective with 80-μm step size, corresponding to Fig. 6. Overall, the five spheres showed a similar profile change (broad-narrow-broad) and the best focus occurred at the fourth row from the top. For the truncated beam and refocused images, the sphere's profiles were all single-peak shaped. For the full beam image however, spheres 1, 4 and 5 showed a profile with sidelobes in the first two rows. Spheres 2 and 3 showed an irregular shape. The behavior of spheres 1, 4 and 5 is consistent with the physical optics simulation (Fig. 3(b)), showing that the lateral profile at the depth between objective and actual focal plane exhibits multiple-maxima. Spheres 2 and 3 do not show this behavior. We hypothesize that spheres 2 and 3 were not exactly centered in the B-scan cross section and therefore were only partially sampled by the full beam.
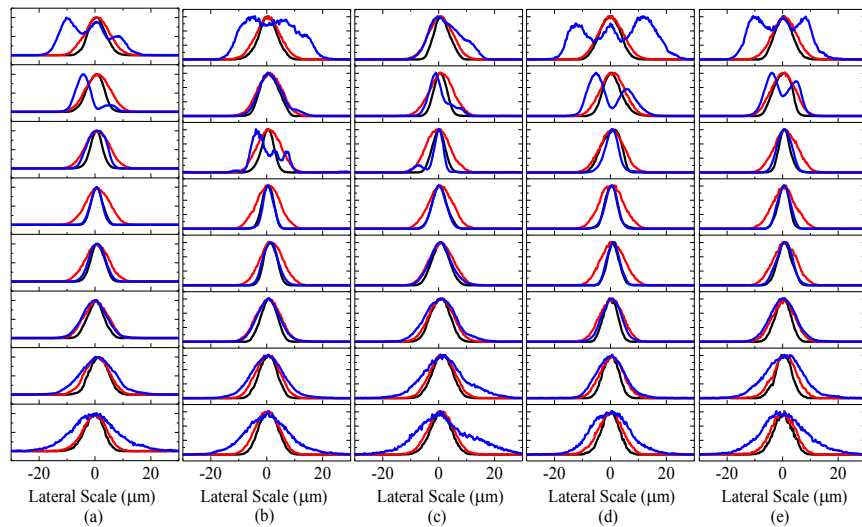

Fig. 7. Lateral intensity profiles of the selected spheres in Fig. 6 for different phantom positions (defocused depths): (a) to (e) are spheres 1 to 5, respectively. The rows from top to bottom represent the different phantom positions with 80-μm step size, corresponding to the images in Fig. 6 from top (Fig. 6(a)) to bottom (Fig. 6(h)). Black: Refocused image; Red: Truncated Gaussian beam image; Blue: Full beam image.

To further quantify the changes discussed above, all the intensity profiles in Fig. 7 were fitted with Gaussian function to determine the full width at half maximum (FWHM). In Figs. 8(a)-8(e) the FWHM is plotted as a function of the phantom displacement relative to the focal plane. Clearly, for all five spheres, the slowest variation in FWHM during defocus occurred for the truncated Gaussian beam image (for this image the resolution is always poor). The most rapid FWHM change is observed for the full beam image. As for the refocused image, it was focused better than the truncated Gaussian beam image over the whole range. This indicates that our refocusing algorithm not only extends the depth-focus as beam truncation does, but also produces better resolution than beam truncation does. As compared to the full beam image, the refocused image yielded a comparable resolution within a short range around actual focal plane. Moreover, the resolution of the refocused image degraded much more

slowly than that of the full beam image. For example, spheres 1 and 5 showed the smallest FWHM in the refocused image and full beam image when the phantom was at around 200 μm. As the phantom position increased from 200 μm, the FWHM increased much more quickly for the full beam image than for the refocused image. To determine the difference in depth-of-focus between the full beam and the refocused beam, the slope of the FWHM as a function of phantom position at the right side of the focus position in Figs. 8(a)-8(e) was determined. On average, the FWHM increase in the full beam image was about 5 times faster than the refocused image.

Figure 8(f) depicts a comparison between the full beam FWHM measured from the experiment and the FWHM calculated from the physical optics simulation. The experimental results match the simulation very well.
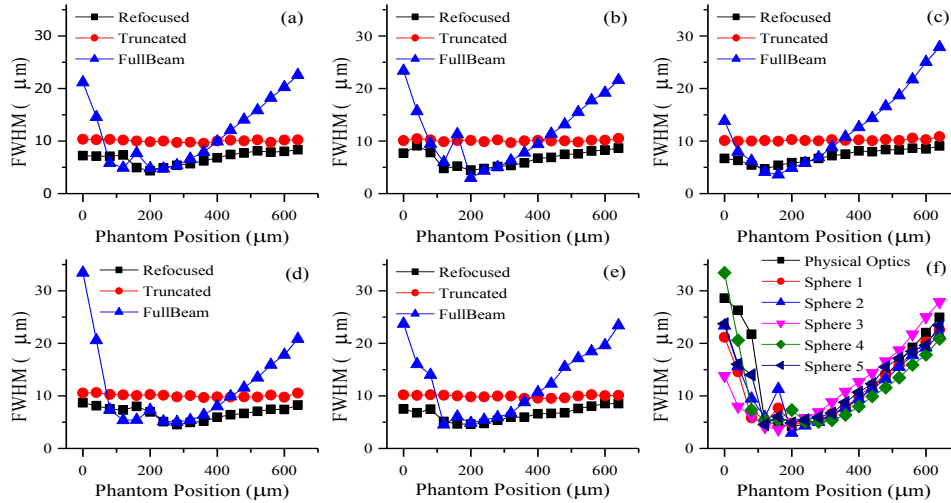

Fig. 8. Full width at half maximum of those selected spheres in Fig. 6 at different defocused depths: (a) Sphere 1, (b) Sphere 2, (c) Sphere 3, (d) Sphere 4, and (e) Sphere 5; (f) FWHM of full beam at different defocused depths from both experiment and physical optics simulation.

To assess the efficiency of the refocusing algorithm in comparison with the truncated beam and the Gaussian beam, the backscattered intensity measured with the OCT system was determined. The energy defined as the backscattered intensity integrated over the area of the five selected spheres was calculated for three imaging modes (i.e., truncated beam, refocused, full beam imaging). In Fig. 9, it is clearly seen that, in truncated beam imaging mode, the five spheres (Figs. 9(a)-9(e)) showed a slow continuous change in energy (increase-maximum-decrease). For the refocused imaging and full beam imaging modes, spheres 2 and 3 show a qualitatively different energy curve than spheres 1, 4 and 5, especially in full beam imaging mode. This behavior is attributed to the assumption that spheres 2 and 3 are only partially sampled by the full beam as noted before. Therefore, these two spheres were excluded from the energy comparison between the refocus imaging and full beam imaging. Spheres 1, 4 and 5 (Figs. 9(a), 9(d) and 9(e)) experienced a very similar energy change over different phantom positions in both the refocused imaging and full beam imaging. Moreover, the energy difference between those two imaging modes was also very consistent among those three spheres.

The energy efficiency of our refocusing algorithm is evaluated on spheres 1, 4 and 5 at three depths around the optimal focus position (phantom at 200, 240, and 280 μm). The results show that our refocusing algorithm suffered only from a −1.9 to −4.1 dB energy efficiency loss as compared to the full beam imaging. This is close to the expected value (−3 dB) based on the theoretical considerations described above. This indicates that our

refocusing method is much more efficient than the depth-of-focus extension by phase-apodization or axicon lens illumination [13, 14]. The fluctuations for the energy measurement are attributed to the well known presence of speckle in OCT images.
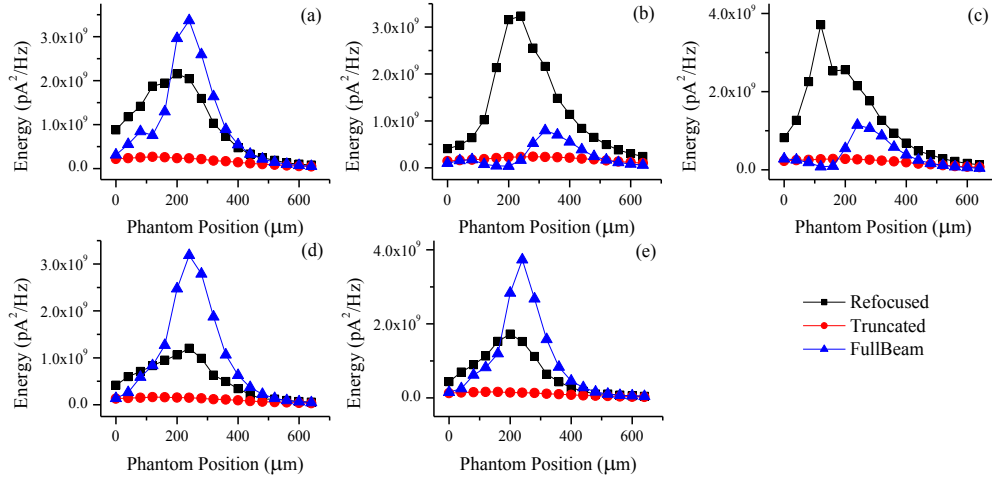

Fig. 9. Scattered energy of the selected spheres in Fig. 6 at different defocused depths: (a) Sphere 1, (b) Sphere 2, (c) Sphere 3, (d) Sphere 4, and (e) Sphere 5. Black: Refocused image; Red: Truncated Gaussian beam image; Blue: Full beam image.
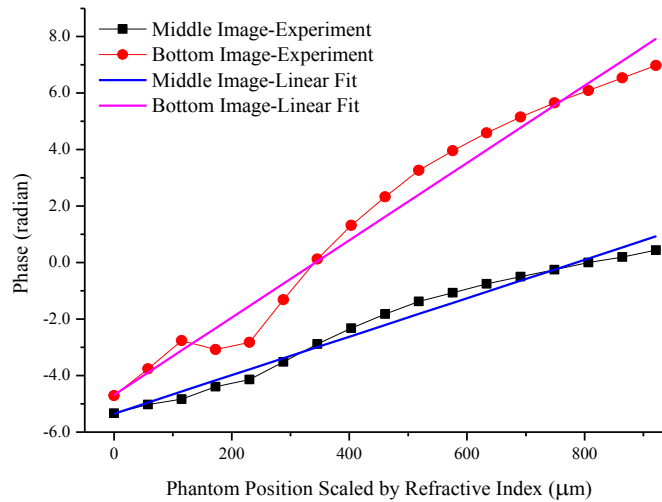

Fig. 10. Phase factor ψ applied to middle and bottom images to optimize the image refocusing. The slopes determined by least square linear fitting are 6.81 and 13.69 mrad/µm, respectively.

Finally, we performed an analysis of the phase factors needed for refocusing. Figure 10 plots the phase factor ψ as a function of defocused depth for both middle and bottom images. The phase factors obtained based on the maximum total backscattered intensity criterion described above showed a linear relationship with the defocused depth, as predicted by theory. Moreover, the slope of the plot for the bottom image was about twice of that for the middle image. The slopes yielded by least square linear fitting are 6.81 and 13.69 mrad/µm. The slope for the middle image (6.81 mrad/µm) is very close to the slope (7.25 mrad/µm) predicted by the physical optics simulation.

5. Summary

In this study, we demonstrated a novel refocusing algorithm to extend the depth-of-focus of OCT imaging using a depth-encoded synthetic aperture. Physical optics simulation results provided an extensive insight into the theory behind the refocusing process. We succeeded to achieve a 5-fold increase in the depth-of-focus compared to full beam imaging. Our refocusing algorithm also yielded a lateral resolution at the focal plane of the objective which is equal to that of the full beam image.

The method is computationally cheap and compatible with endoscopic-OCT, showing a great potential to be integrated into real-time miniature catheter-based endoscopic OCT systems [20]. With the availability of long coherence length laser sources exceeding 10 mm [21], depth encoded synthetic aperture OCT becomes feasible for *in vivo* tissue imaging.

The method can be extended even further by creating additional depth encoded apertures. We expect that this will improve the refocusing results even further. However, the depth range needed to depth encode more apertures increases rapidly.

Acknowledgment